Available online at www.sciencedirect.com
SCIENCE DIRECT
Journal of Sound and Vibration 296 (2006) 1013–1027
JOURNAL OF SOUND AND VIBRATION
www.elsevier.com/locate/jsvi

Short Communication

Flexural wave propagation and power flow in an axisymmetrical circular plate by the acoustical wave propagator technique ☆

S.Z. Peng[a,*], J. Pan[b]

[a] *Department of Mechanical Engineering, The Hong Kong Polytechnic University, Hung Hom, Kowloon, Hong Kong*
[b] *Centre for Acoustics, Dynamics and Vibration, School of Mechanical Engineering, The University of Western Australia, 35 Stirling HWY, Crawley, WA 6009, Australia*

Received 8 August 2005; accepted 31 January 2006
Available online 30 May 2006

Abstract

This paper presents the acoustical wave propagator (AWP) technique to describe the time-dependent flexural wave propagation, dynamic stress and power flow in an axisymmetrical circular plate. A combined scheme of Chebyshev polynomial expansion and fast Fourier transformation is used to implement the operation of the AWP in polar coordinates. The exact analytical solution of plate vibration velocity is used to compare with those obtained by the AWP technique to verify its validity. Kinetic, potential and total energy densities, and power intensity are also studied for better understanding of energy and power flow distributions in vibrating circular plate.

1. Introduction

Thin circular plates are extensively used in mechanical, air/space and maritime industries as the basic structural components, such as a circular mounting plate that attaches to the Slim Armstrong and Universal Mounting System. Much numerical work has been carried out for analysing the axisymmetrical vibration of circular plates. Pardoen and Hagen [1] and Pardoen [2] discussed the static, vibration and bending analysis of axisymmetrical circular plates using the finite element method. Schmidt and Krenk [3] investigated the asymmetric problem of a vibrating circular elastic plate on an elastic half-space by an integral equation method. Later, Chang [4] presented statistical analysis of a circular plate on a random winkler support using the small fluctuation approximation approach. Chang [5] investigated the axisymmetrical buckling of moderately thick polar orthotropic annular plates. Mermertas and Belek [6] studied the static and dynamic stability of variably thick orthotropic annular plates subjected to in-plate periodic forces. Roy and Ganesan [7] concerned dynamic stress analysis of a tapered clamped-free annular circular plate under axisymmetrical impact load. Recently, Wang [8] derived the relationships between Midlin and Kirchhoff bending solutions for tapered circular and annular plates. Liew et al. [9] described the vibration analysis of circular Mindlin plates

☆ Presented in part at the 18th International Congress on Acoustics, April 4–9, Kyoto, Japan, 2004.

*Corresponding author. Tel.: +852 2766 6664; fax: +852 2365 4703.
E-mail addresses: mmszpeng@polyu.edu.hk (S.Z. Peng), pan@mech.uwa.edu.au (J. Pan).

0022-460X/$ - see front matter © 2006 Elsevier Ltd. All rights reserved.
doi:10.1016/j.jsv.2006.01.072

using the differential quadrature method. Chang and Lee [10] solved large deformation problems in a circular plate using the double-side method.

However, considerable studies mentioned above have been focused on the vibration analysis in the frequency domain, only a few of researchers investigated wave propagation and dynamic stress concentration of a circular plate. Hence, it is necessary to develop an effective and accurate time-domain numerical method for studying the axisymmetrical flexural wave propagation, stress distribution and power flow in vibrating circular plates. Most recently, Peng and Pan extended the acoustical wave propagator (AWP) method developed by Pan and Wang [11] to describe the wave propagation in a thin plate [12], dynamic stress concentration in a stepped plate [13], a ribbed plate [14] and a heterogeneous plate with multiple cylindrical patches [15]. The previous papers of Peng and Pan are limited to structures in rectangular coordinates. The main objective of this paper is to investigate wave propagation and dynamic stress distribution, and effects of kinetic and potential energies on total energy densities, and power intensity in a circular plate. The analysis and study provide a better understanding on dynamic stress and energy distributions in circular plates.

2. Theory of the AWP technique in polar coordinates

2.1. Derivatives of the AWP $e^{-(t-t_0)\hat{\mathbf{H}}}$ in polar coordinates

Fig. 1 shows a circular plate structure as common components of many practical engineering structures such as the above-mentioned specific example. In this paper, the classical Kirchhoff's thin plate theory is used to investigate wave propagation and power flow. When the plate is suddenly disturbed by an axisymmetrical impact load, which can be defined as an initial displacement, the wave motion cause dynamic moments and shear forces, which generate internal stresses.

The stresses can be calculated by [16]

$$\sigma_r = -\frac{Eh}{2(1-\upsilon^2)}\left\{\frac{\partial^2 w}{\partial r^2}+\frac{\upsilon}{r}\frac{\partial w}{\partial r}\right\}, \quad \sigma_\theta = -\frac{Eh}{2(1-\upsilon^2)}\left\{\frac{1}{r}\frac{\partial w}{\partial r}+\upsilon\frac{\partial^2 w}{\partial r^2}\right\}, \quad \sigma_{r\theta}=0, \tag{1}$$

where $w(r,t)$ represents the deflection displacement of the plate in the z direction; E, h and υ denote the Young's modulus, thickness and Poisson's ratio of the circular plate, respectively.

The maximum stress is calculated by

$$\sigma_{\max} = \max\{\sigma_r, \sigma_\theta\}. \tag{2}$$

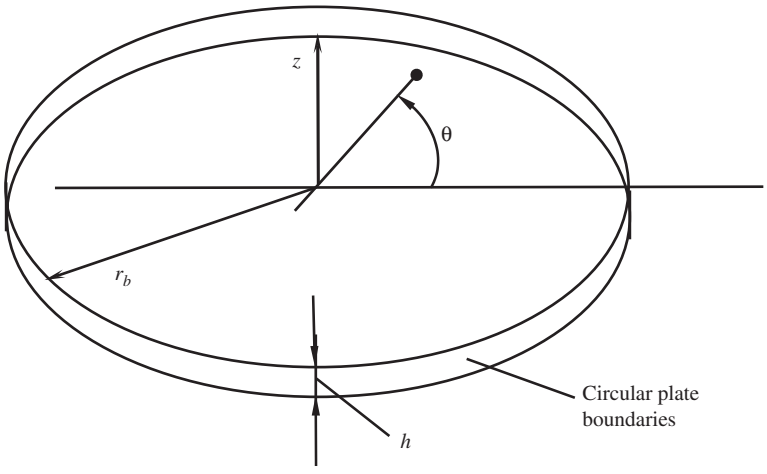

Fig. 1. Schematic of a circular plate structure.

The bending moments and twisting moment, and shear forces are given, in polar coordinates, as

$$M_r = -D\left\{\frac{\partial^2 w}{\partial r^2}+\frac{\upsilon}{r}\frac{\partial w}{\partial r}\right\}, \quad M_\theta = -D\left\{\upsilon\frac{\partial^2 w}{\partial r^2}+\frac{1}{r}\frac{\partial w}{\partial r}\right\}, \quad M_{r\theta}=0,$$
$$Q_r = -D\frac{\partial}{\partial r}\left[\nabla^2 w\right] = -D\left[\frac{\partial^3 w}{\partial r^3}+\frac{1}{r}\frac{\partial^2 w}{\partial r^2}-\frac{1}{r^2}\frac{\partial w}{\partial r}\right], \quad Q_\theta = 0, \tag{3}$$

where

$$\nabla^2 = \frac{\partial^2}{\partial r^2}+\frac{1}{r}\frac{\partial}{\partial r}, \quad D=\frac{Eh^3}{12(1-\upsilon^2)}$$

is the flexural rigidity of the circular plate; and Q_r and Q_θ are transverse shear forces.

The derivative of the shear force in the radial direction is

$$\frac{\partial Q_r}{\partial t} = -D\left[\frac{\partial^3 V}{\partial r^3}+\frac{1}{r}\frac{\partial^2 V}{\partial r^2}-\frac{1}{r^2}\frac{\partial V}{\partial r}\right], \tag{4}$$

where $V(r,t)$ is the velocity of the plate ($V=\partial w/\partial t$).

The governing equation for motion of this structure in polar coordinates is given by

$$\rho_s h\frac{\partial^2 w(r,t)}{\partial t^2}+D\nabla^4 w(r,t)=0, \tag{5}$$

where

$$\nabla^4 w = \frac{\partial^4 w}{\partial r^4}+\frac{1}{r^3}\frac{\partial w}{\partial r}-\frac{1}{r^2}\frac{\partial^2 w}{\partial r^2}+\frac{2}{r}\frac{\partial^3 w}{\partial r^3}$$

and ρ_s is the mass per unit area of the plate.

The system state equation can be described by the following wave equation:

$$\frac{\partial}{\partial t}\Phi(r,t) = -\hat{\mathbf{H}}\Phi(r,t), \tag{6}$$

where $\Phi(r,t)$ is a state vector representing the velocity V and shear force Q_r in the radial direction, and is defined as

$$\Phi(r,t) = \begin{bmatrix} V \\ Q_r \end{bmatrix} \tag{7}$$

and $\hat{\mathbf{H}}$ is the system operator defined as

$$\hat{\mathbf{H}} = \begin{bmatrix} 0 & -\frac{1}{\rho_s h}\left(\frac{\partial}{\partial r}+\frac{1}{r}\right) \\ D\left(\frac{\partial^3}{\partial r^3}+\frac{\upsilon}{r}\frac{\partial^2}{\partial r^2}-\frac{\upsilon}{r^2}\frac{\partial}{\partial r}\right) & 0 \end{bmatrix}. \tag{8}$$

Eq. (6) can be rewritten by integrating with respect to time

$$\Phi(r,t) = \mathrm{e}^{-(t-t_0)\hat{\mathbf{H}}}\Phi(r,t_0), \tag{9}$$

where $\mathrm{e}^{-(t-t_0)\hat{\mathbf{H}}}$ is the AWP and $\Phi(r,t_0)$ denotes the initial state vector.

Through the operation of the AWP $\mathrm{e}^{-(t-t_0)\hat{\mathbf{H}}}$ acting upon the initial state vector, we can obtain the state vector $\Phi(r,t)$ of acoustical waves at any time t and at any position. It is noted that the system operator $\hat{\mathbf{H}}$ includes readily the effect of boundaries and spatial variation of the acoustical media due to the material properties defined as a function of position.

2.2. Implementation of the AWP $e^{-(t-t_0)\hat{\mathbf{H}}}$ in polar coordinates

The crucial step in the numerical implementation is the development of an efficient algorithm for performing the operation of the AWP. The Chebyshev polynomial expansion (CPE) scheme has the significant advantage that it allows the use of the very long time step. Meanwhile, this scheme has an exponential convergent rate. More detailed accounts can be found in Refs. [12,13]. In this section, real Chebyshev polynomials defined in the ranges of $[-1,1]$ are used in the expansion of the AWP, so the system operation $\hat{\mathbf{H}}$ needs to be normalised by $\hat{\mathbf{H}}' = \hat{\mathbf{H}}/\sqrt{\lambda_{\max}}$, where $\lambda_{\max}$ represents the maximum eigenvalue of the system operator $\hat{\mathbf{H}}$.

Using Chebyshev polynomials of the first kind, Eq. (9) can be further rewritten as

$$\phi(r,t) = \sum_{n=0}^{\infty} a_n(R) T_n(\hat{\mathbf{H}}')\phi(r,t_0), \tag{10}$$

where $R = \sqrt{\lambda_{\max}}(t—t_0)$; $a_n(R) = 2I_n(R)$ except $a_0(R) = I_0(R)$ and $I_n(R)$ is the nth-order modified Bessel function of the first kind. The zero- and first-order Chebyshev polynomials are defined as $T_0\left(\hat{\mathbf{H}}'\right) = \mathbf{I}$ and $T_1\left(\hat{\mathbf{H}}'\right) = \hat{\mathbf{H}}'$, and the remainder terms can be calculated by the following recursive formula:

$$T_{n+1}\left(\hat{\mathbf{H}}'\right) = 2\hat{\mathbf{H}}' T_n\left(\hat{\mathbf{H}}'\right) - T_{n-1}\left(\hat{\mathbf{H}}'\right). \tag{11}$$

Due to $\hat{\mathbf{H}}'$ as a function of the spatial derivatives, the following Fourier transformation and its inverse transformation is used to calculate the spatial derivatives of function $\Phi(r,t)$:

$$\frac{\partial^n}{\partial r^n}\phi(r,t) = F^{-1}\left\{(\mathrm{j}k_r)^n F[\phi(r,t)]\right\}, \tag{12}$$

where $n = 1$, 2 and 3; $F^{-1}\{\}$ and $F[]$ represent the inverse Fourier transformation and Fourier transformation, respectively; and k_r is the bending wave number as in $e^{\mathrm{j}k_r r}$.

The error analysis of the Fourier transformation method for the spatial derivatives has been given in Refs. [11,12] to compare with other numerical schemes. The sampling interval is chosen to represent the highest frequency component of interest in the medium, where the shortest wavelength is supported. When the spatial sampling interval Δr is given, the discrete Fourier expansion of a wave packet supports the maximum wave number. Therefore, the normalisation factor R can be calculated by

$$R = \sqrt{\frac{Eh^2}{12\rho(1-\upsilon^2)}}\left[\left(\frac{\pi}{\Delta r}\right)^2 + \frac{1}{r}\left(\frac{\pi}{\Delta r}\right)\right](t-t_0). \tag{13}$$

2.3. Power intensity and energy density in polar coordinates

The kinetic energy intensity per unit area is given by

$$E_k = \frac{1}{2}\rho_s\left(\frac{\partial w}{\partial t}\right)^2. \tag{14}$$

The potential energy density is given by

$$E_p = \frac{1}{2}D\left[\left(\frac{\partial^2 w}{\partial r^2}\right)^2 + \frac{1}{r^2}\left(\frac{\partial w}{\partial r}\right)^2 + \frac{2\upsilon}{r}\left(\frac{\partial^2 w}{\partial r^2}\right)\left(\frac{\partial w}{\partial r}\right)\right]. \tag{15}$$

Therefore, the total vibration energy density is the sum of Eqs. (14) and (15)

$$E_t = E_k + E_p = \frac{1}{2}\left\{\rho_s\left(\frac{\partial w}{\partial t}\right)^2 + D\left[\left(\frac{\partial^2 w}{\partial r^2}\right)^2 + \frac{1}{r^2}\left(\frac{\partial w}{\partial r}\right)^2 + \frac{2\upsilon}{r}\left(\frac{\partial^2 w}{\partial r^2}\right)\left(\frac{\partial w}{\partial r}\right)\right]\right\}. \tag{16}$$

The power intensity I_r is defined as

$$I_r = Q_r \frac{\partial w}{\partial t} + M_r \frac{\partial}{\partial r}\left(\frac{\partial w}{\partial t}\right). \tag{17}$$

The relationship between the power intensity and energy density can be described as

$$I_r = C_r E, \tag{18}$$

where C_r is called the coefficient of the power intensity and energy density.

If we consider a typical unit Gaussian wave packet

$$w(r,t) = \frac{1}{1+\tau^2} e^{(-\mu^2/(1+\tau^2))}\left\{\cos\left(\frac{\mu^2\tau}{1+\tau^2}\right) + \tau \sin\left(\frac{\mu^2\tau}{1+\tau^2}\right)\right\}, \tag{19}$$

where $\tau = bt/\sigma^2$, $\mu = r/2\sigma$. $w(r,t)$ and σ represent the deflection displacement of the plate in the z-axis and Gaussian factor, respectively.

The first-order derivative of $w(r,t)$ with time is given by

$$\frac{\partial w}{\partial t} = \frac{b}{\sigma^2(1+\tau^2)^3} e^{(-\mu^2/(1+\tau^2))}\left\{\zeta_1 \cos\left(\frac{\mu^2\tau}{1+\tau^2}\right) + \zeta_2 \sin\left(\frac{\mu^2\tau}{1+\tau^2}\right)\right\}, \tag{20}$$

where

$$\begin{aligned}\zeta_1 &= \left[2\tau\left(\mu^2 - 1 - \tau^2\right) + \tau\mu^2\left(1-\tau^2\right)\right],\\ \zeta_2 &= \left\lfloor 2\tau^2\left(\mu^2 - 1 - \tau^2\right) + \left(1+\tau^2\right)^2 - \mu^2\left(1-\tau^2\right)\right\rfloor.\end{aligned} \tag{21}$$

Therefore, the kinetic energy can be calculated by

$$E_k = \frac{b^2\rho_s}{2\sigma^4(1+\tau^2)^6} e^{(-2\mu^2/(1+\tau^2))}\left\{\zeta_1 \cos\left(\frac{\mu^2\tau}{1+\tau^2}\right) + \zeta_2 \sin\left(\frac{\mu^2\tau}{1+\tau^2}\right)\right\}^2. \tag{22}$$

The derivative of $\partial w/\partial t$ is given by

$$\frac{\partial}{\partial r}\left(\frac{\partial w}{\partial t}\right) = \frac{b\mu}{\sigma^3(1+\tau^2)^4} e^{(-\mu^2/(1+\tau^2))}\left\{\zeta_3 \cos\left(\frac{\mu^2\tau}{1+\tau^2}\right) + \zeta_4 \sin\left(\frac{\mu^2\tau}{1+\tau^2}\right)\right\}, \tag{23}$$

where

$$\begin{aligned}\zeta_3 &= \left\lfloor -\zeta_1 + \tau\left(1+\tau^2\right)\left(3-\tau^2\right) + \zeta_2\tau\right\rfloor,\\ \zeta_4 &= \left\lfloor -\zeta_2 + \left(1+\tau^2\right)\left(3\tau^2-1\right) - \zeta_1\tau\right\rfloor.\end{aligned} \tag{24}$$

The first-order derivative of $W(r,t)$ is given by

$$\frac{\partial W(r,t)}{\partial r} = \frac{\mu}{\sigma(1+\tau^2)^2} e^{(-\mu^2/(1+\tau^2))}\left\{(\tau^2-1)\cos\left(\frac{\mu^2\tau}{1+\tau^2}\right) - 2\tau \sin\left(\frac{\mu^2\tau}{1+\tau^2}\right)\right\}. \tag{25}$$

The second-order derivative of $W(r,t)$ is given by

$$\frac{\partial^2 W(r,t)}{\partial r^2} = \frac{1}{2\sigma^2(1+\tau^2)^3} e^{(-\mu^2/(1+\tau^2))}\left\{\zeta_5 \cos\left(\frac{\mu^2\tau}{1+\tau^2}\right) + \zeta_6 \sin\left(\frac{\mu^2\tau}{1+\tau^2}\right)\right\}, \tag{26}$$

where

$$\zeta_5 = \tau^4 - 6\mu^2\tau^2 + 2\mu^2 - 1$$

and

$$\zeta_6 = 2\tau\left(3\mu^2 - \mu^2\tau^2 - 1 - \tau^2\right).$$

The third-order derivative of $W(r,t)$ is given by

$$\frac{\partial^3 W(r,t)}{\partial r^3} = \frac{\mu}{2\sigma^3(1+\tau^2)^4} e^{(-\mu^2/(1+\tau^2))} \left\{ \zeta_7 \cos\left(\frac{\mu^2\tau}{1+\tau^2}\right) + \zeta_8 \sin\left(\frac{\mu^2\tau}{1+\tau^2}\right) \right\}, \tag{27}$$

where

$$\begin{aligned} \zeta_7 &= 12\mu^2\tau^2 - 9\tau^4 - 2\mu^2 - 6\tau^2 - 2\mu^2\tau^4 + 3, \\ \zeta_8 &= -8\tau\mu^2 + 8\tau^3\mu^2 + 9\tau - 3\tau^5 + 6\tau^3. \end{aligned} \tag{28}$$

The shear force and bending moment in the radial direction can be calculated by

$$\begin{aligned} M_r &= \frac{-D}{2\sigma^2(1+\tau^2)^3 r} e^{(-\mu^2/(1+\tau^2))} \left\{ \zeta_{M1} \cos\left(\frac{\mu^2\tau}{1+\tau^2}\right) + \zeta_{M2} \sin\left(\frac{\mu^2\tau}{1+\tau^2}\right) \right\}, \\ Q_r &= \frac{-D}{2\sigma^3(1+\tau^2)^4 r^2} e^{(-\mu^2/(1+\tau^2))} \left\{ \zeta_{Q1} \cos\left(\frac{\mu^2\tau}{1+\tau^2}\right) + \zeta_{Q2} \sin\left(\frac{\mu^2\tau}{1+\tau^2}\right) \right\}, \end{aligned} \tag{29}$$

$$\begin{aligned} \zeta_{M1} &= 2\mu\sigma\upsilon(\tau^4 - 1) + r\zeta_5, \quad \zeta_{M2} = -4\mu\upsilon\sigma\tau(1+\tau^2) + r\zeta_6, \\ \zeta_{Q1} &= \mu r^2\zeta_7 + \sigma r(1+\tau^2)\zeta_5 - 2\mu\sigma^2(1+\tau^2)(\tau^4 - 1), \\ \zeta_{Q2} &= \mu r^2\zeta_8 + \sigma r(1+\tau^2)\zeta_6 + 4\mu\tau\sigma^2(1+\tau^2)^2. \end{aligned} \tag{30}$$

Similarly, the potential energy density can be calculated by

$$E_p = \frac{D}{8\sigma^4 r^2(1+\tau^2)^6} e^{(-2\mu^2/(1+\tau^2))} \left\{ \zeta_9 \cos^2\left(\frac{\mu^2\tau}{1+\tau^2}\right) + \zeta_{10} \sin\left(\frac{2\mu^2\tau}{1+\tau^2}\right) + \zeta_{11} \sin^2\left(\frac{\mu^2\tau}{1+\tau^2}\right) \right\}, \tag{31}$$

where

$$\begin{aligned} \zeta_9 &= r^2\zeta_5^2 + 4\sigma^2(\tau^4 - 1)^2\mu^2 + 4\mu r\sigma\upsilon\zeta_5(\tau^4 - 1), \\ \zeta_{10} &= r^2\zeta_5\zeta_6 - 8\sigma^2(\tau^4 - 1)(\tau^2 + 1)\tau\mu^2 + 2\mu r\sigma\upsilon(\tau^2 + 1)[\zeta_6(\tau^2 - 1) - 2\zeta_5\tau], \\ \zeta_{11} &= r^2\zeta_6 + 16\sigma^2(\tau^2 + 1)^2\mu^2\tau^2 - 8\mu r\sigma\upsilon\zeta_6\tau(\tau^2 + 1). \end{aligned} \tag{32}$$

Therefore, the total energy under the initial Gaussian wave packet with unit magnitude

$$E = \frac{1}{8\sigma^4 r^2(1+\tau^2)^6} e^{(-2\mu^2/(1+\tau^2))} \left\{ \zeta_{12} \cos^2\left(\frac{\mu^2\tau}{1+\tau^2}\right) + \zeta_{13} \sin\left(\frac{2\mu^2\tau}{1+\tau^2}\right) + \zeta_{14} \sin^2\left(\frac{\mu^2\tau}{1+\tau^2}\right) \right\}, \tag{33}$$

where

$$\zeta_{12} = 4r^2b^2\rho_s\zeta_1^2 + D\zeta_9, \quad \zeta_{13} = 4r^2b^2\rho_s\zeta_1\zeta_2 + D\zeta_{10}, \quad \zeta_{14} = 4r^2b^2\rho_s\zeta_2^2 + D\zeta_{11}. \tag{34}$$

The power intensity I_r is calculated by

$$I_r = \frac{-Db}{2\sigma^5(1+\tau^2)^7} e^{(-2\mu^2/(1+\tau^2))} \left\{ \zeta_{I1} \cos^2\left(\frac{\mu^2\tau}{1+\tau^2}\right) + \zeta_{I2} \sin\left(\frac{2\mu^2\tau}{1+\tau^2}\right) + \zeta_{I3} \sin^2\left(\frac{\mu^2\tau}{1+\tau^2}\right) \right\}, \tag{35}$$

where

$$\zeta_{I1} = \zeta_1\zeta_{Q1} + \mu r\zeta_3\zeta_{M1}, \quad \zeta_{I2} = \frac{\zeta_1\zeta_{Q2} + \zeta_2\zeta_{Q1} + \mu r(\zeta_3\zeta_{M2} + \zeta_4\zeta_{M1})}{2}, \quad \zeta_{I3} = \zeta_2\zeta_{Q2} + \mu r\zeta_4\zeta_{M2}. \tag{36}$$

Finally, the coefficient of the power intensity and energy density C_r is given by

$$C_r = \frac{-4Dbr^2\{\zeta_{I1}\cos^2(\mu^2\tau/1+\tau^2) + \zeta_{I2}\sin(2\mu^2\tau/1+\tau^2) + \zeta_{I3}\sin^2(\mu^2\tau/1+\tau^2)\}}{\sigma(1+\tau^2)\{\zeta_{12}\cos^2(\mu^2\tau/1+\tau^2) + \zeta_{13}\sin(2\mu^2\tau/1+\tau^2) + \zeta_{14}\sin^2(\mu^2\tau/1+\tau^2)\}}. \tag{37}$$

The physical meaning about C_r is further termed the group velocity, which is used to describe not only the relationship between the power intensity and energy density, but also the gradient of the dispersion

relationship $\partial\omega/\partial k$ between the angular frequency ω and wave number k. Furthermore, it quantifies the speed at which energy is transported by the dispersive wave. It is the velocity at which an amplitude function which is impressed upon a carrier wave packet (a time-varying wave motion which can be represented as a summation of numerous harmonic waves) travels, and it is of great physical importance.

2.4. Exact analytical solutions in polar coordinates

The exact analytical solutions are used to assess the prediction accuracy of the Chebyshev–Fourier scheme developed in the previous section. The displacement of an axisymmetrical circular plate has the following analytical solution [16]:

$$W(r,t)=\frac{f_0}{1+\tau^2}\mathrm{e}^{(-\mu^2/(1+\tau^2))}\left\{\cos\left(\frac{\mu^2\tau}{1+\tau^2}\right)+\tau\,\sin\left(\frac{\mu^2\tau}{1+\tau^2}\right)\right\}, \tag{38}$$

where $\tau=bt/\sigma^2, \mu=r/2\sigma$, the coefficient b can be calculated by $\sqrt{Eh^2/12\rho(1-\upsilon^2)}$. $W(r,t)$, σ and f_0 represent the deflection displacement of the plate in the z-axis, Gaussian factor and a constant, respectively.

According to the first- and second-order derivatives of $W(r,t)$, the bending moments and stresses are, respectively, given by

$$\begin{aligned}M_r&=-\frac{Df_0}{2\sigma(1+\tau^2)^2}\mathrm{e}^{(-\mu^2/(1+\tau^2))}\left\{B_1\,\cos\left(\frac{\mu^2\tau}{1+\tau^2}\right)+B_2\,\sin\left(\frac{\mu^2\tau}{1+\tau^2}\right)\right\},\\ M_\theta&=-\frac{Df_0}{2\sigma(1+\tau^2)^2}\mathrm{e}^{(-\mu^2/(1+\tau^2))}\left\{B_3\,\cos\left(\frac{\mu^2\tau}{1+\tau^2}\right)+B_4\,\sin\left(\frac{\mu^2\tau}{1+\tau^2}\right)\right\},\end{aligned} \tag{39}$$

and

$$\begin{aligned}\sigma_r&=-\frac{Ehf_0}{4\sigma(1-\upsilon^2)(1+\tau^2)^2}\mathrm{e}^{(-\mu^2/(1+\tau^2))}\left\{B_1\,\cos\left(\frac{\mu^2\tau}{1+\tau^2}\right)+B_2\,\sin\left(\frac{\mu^2\tau}{1+\tau^2}\right)\right\},\\ \sigma_\theta&=-\frac{Ehf_0}{4\sigma(1-\upsilon^2)(1+\tau^2)^2}\mathrm{e}^{(-\mu^2/(1+\tau^2))}\left\{B_3\,\cos\left(\frac{\mu^2\tau}{1+\tau^2}\right)+B_4\,\sin\left(\frac{\mu^2\tau}{1+\tau^2}\right)\right\},\end{aligned} \tag{40}$$

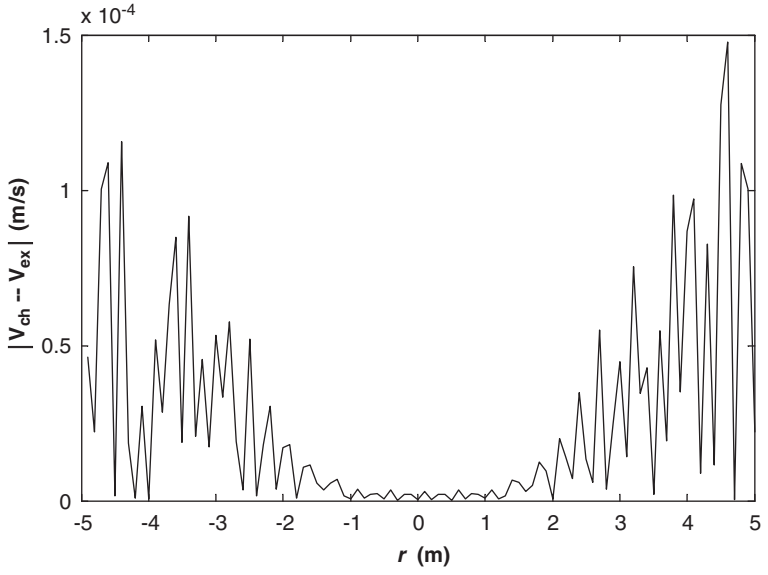

Fig. 2. Absolute error of velocity between the predictions of the Chebyshev scheme and exact solution when $r=0-5$ m and $t=0.034$ s.

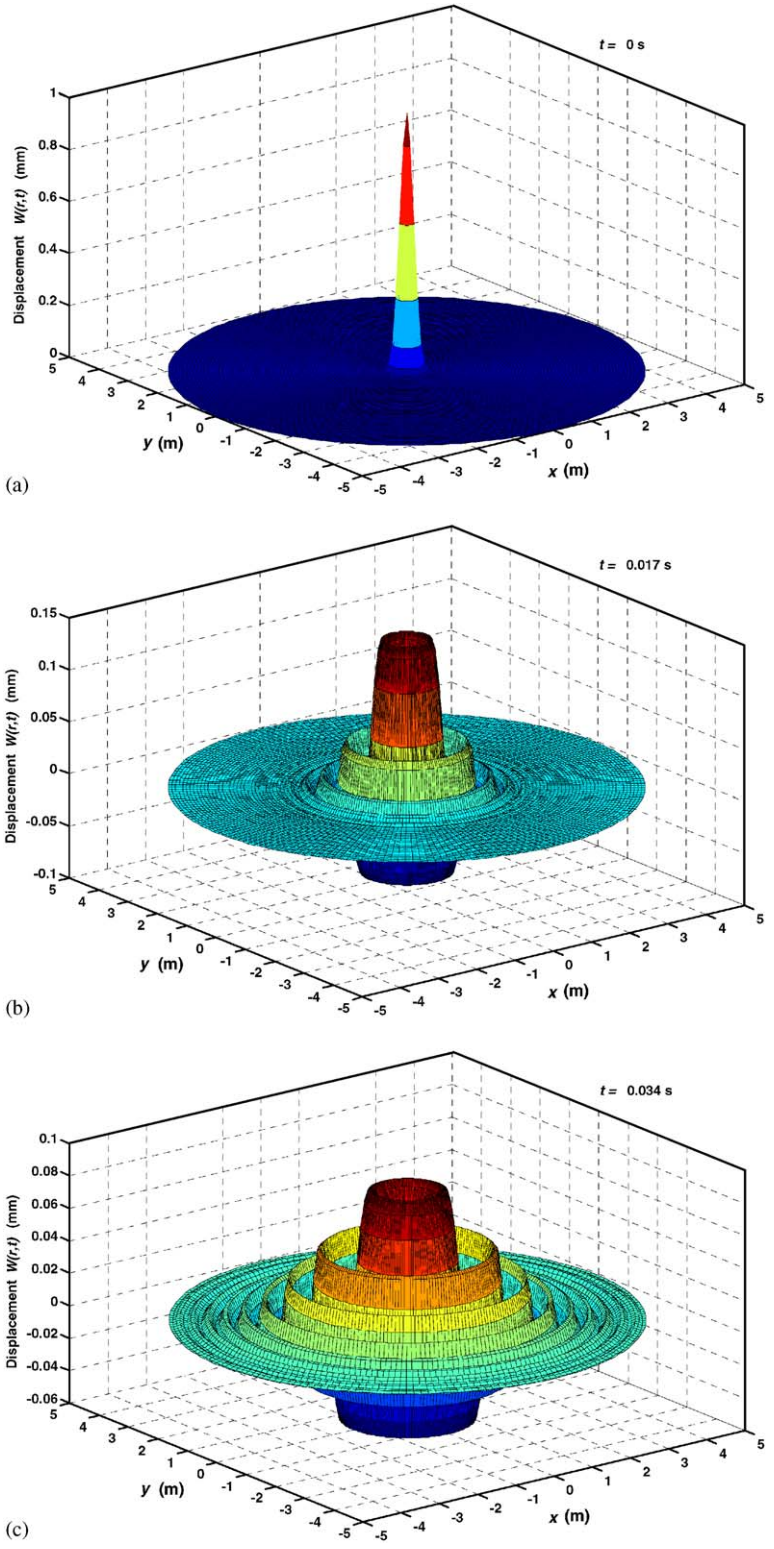

Fig. 3. Distributed flexural wave displacement at different instants by the AWP technique.

where

$$B_1 = \frac{r(\tau^4 - 6\tau^2\mu^2 + 2\mu^2 - 1) + 2\upsilon\mu\sigma(\tau^4 - 1)}{\sigma(1+\tau^2)^2 r}, \quad B_2 = \frac{2\tau r(3\mu^2 - \mu^2\tau^2 - 1 - \tau^2) - 4\upsilon\mu\sigma\tau(1+\tau^2)}{\sigma(1+\tau^2)^2 r},$$
$$B_3 = \frac{\upsilon r(\tau^4 - 6\tau^2\mu^2 + 2\mu^2 - 1) + 2\mu\sigma(\tau^4 - 1)}{\sigma(1+\tau^2)^2 r}, \quad B_4 = \frac{2\upsilon\tau r(3\mu^2 - \mu^2\tau^2 - 1 - \tau^2) - 4\mu\sigma\tau(1+\tau^2)}{\sigma(1+\tau^2)^2 r}. \quad (41)$$

It is noted that the stresses in Eq. (40) have the same distributions as the related moments in Eq. (39) except the difference in magnitude. The maximum stress can be calculated by Eq. (2).

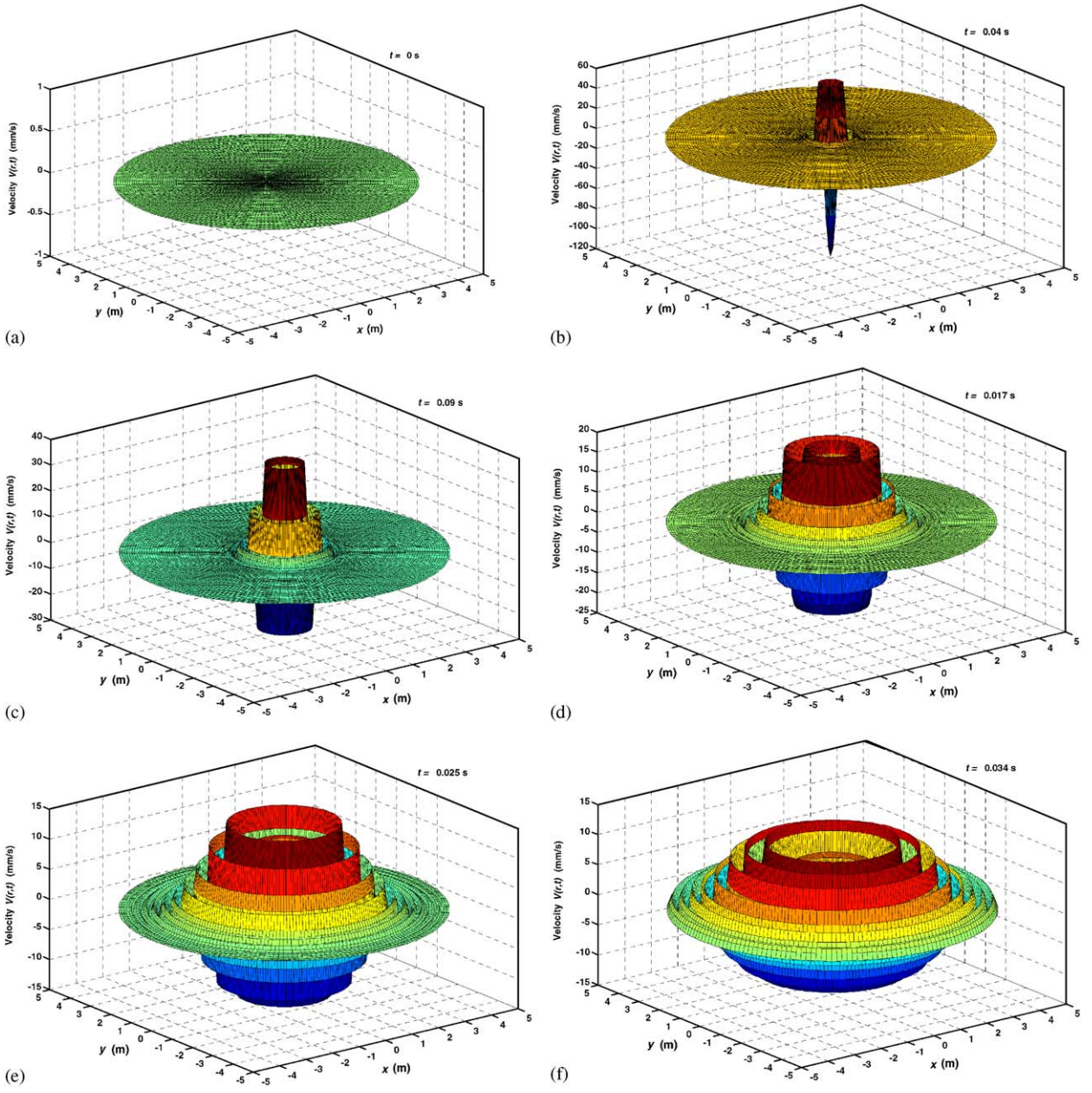

Fig. 4. Distributed flexural wave velocity at different instants by the AWP technique.

3. Results and discussion

The predicted results of velocity by the Chebyshev–Fourier scheme are compared with those obtained by the exact analytical solutions. A good agreement as shown in Fig. 2 shows that the Chebyshev–Fourier scheme can be accurately used to predict the flexural wave propagation. The AWP technique is applied to investigate the flexural wave propagation and power flow in a circular plate. Its material properties are $E = 21.6 \times 10^{10}\,\mathrm{N/m^2}$, $v = 0.3$ and $\rho = 7800\,\mathrm{kg/m^3}$. The thickness and radius of the circular plate are 0.002 and 5 m, respectively.

The following initial state vector is chosen to demonstrate the application of the AWP

$$\phi(r,0) = \begin{bmatrix} 0 \\ Q_r(r,0) \end{bmatrix}, \tag{42}$$

where $Q_r(r, 0)$ is related to the initial displacement $W(r,0) = W_0 e^{-r^2/4\sigma^2}$. Other simulated parameters are given as follows: $W_0 = 0.001$ m, $\sigma = 0.1$, the number of grid points $N_r = N_\theta$ are 100. The spatial sampling intervals Δr and $\Delta\theta$ are 0.1 m and 3.6°, respectively. The evolution of wave packet and reflected waves with different boundaries is observed with $r = 5$ m.

Fig. 3 shows the distributed flexural wave displacement at different instants by the AWP technique. In addition, velocity distribution is very important to investigate the energy and power flow distribution in the structure. Fig. 4 shows the distributed flexural wave velocity at different instants by the AWP technique. At $t = 0$ s, the initial velocity is zero, as illustrated in Fig. 4(a). After a very short time, for example, $t = 0.004$ s, around the centre of the circular plate, velocity has a very large negative magnitude (like a sharp impulse),

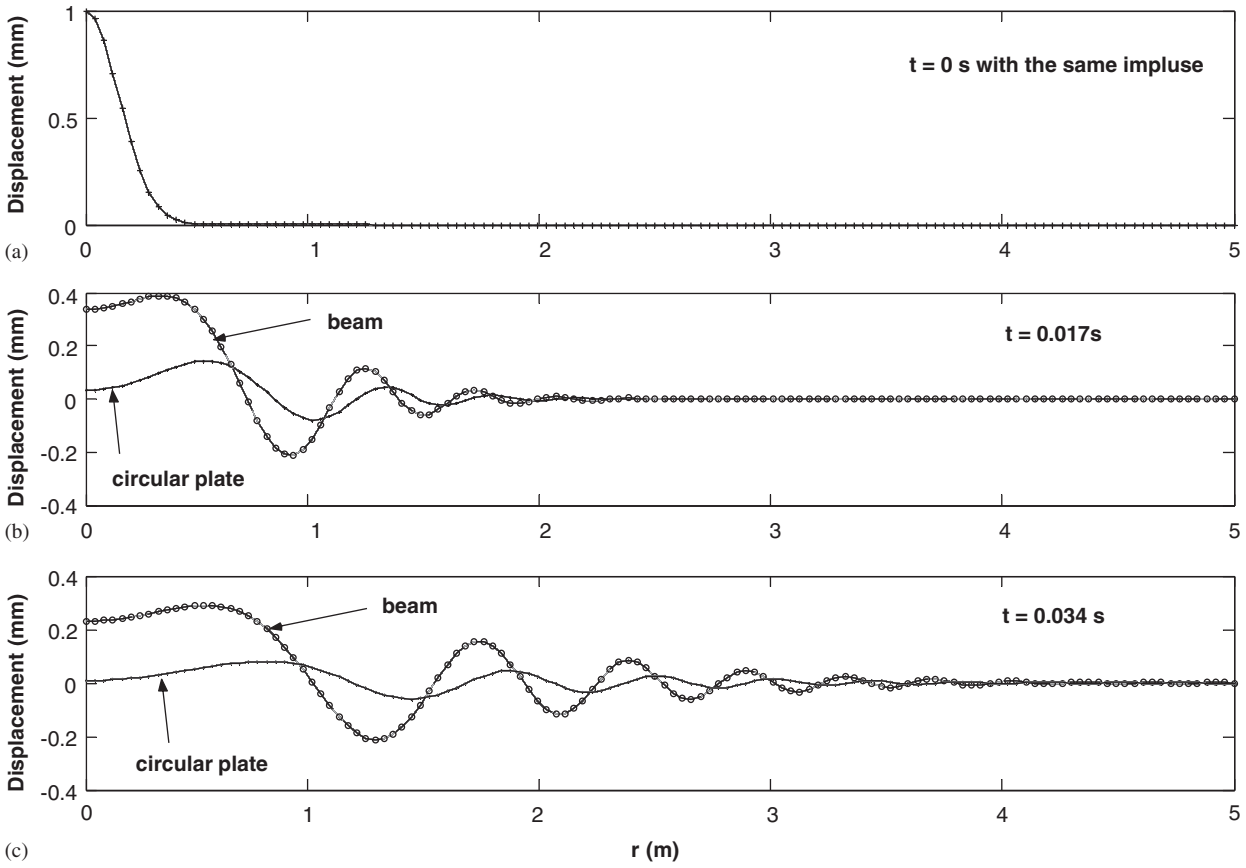

Fig. 5. Distributed flexural wave displacement between the circular plate and the one-dimensional flexural beam at several different instants.

as clearly shown in Fig. 4(b). The velocity distribution is much different from the displacement distribution (Fig. 3), which has the largest magnitude at the initial condition and gradually spreads out with decreased magnitude. As time increases, the negative components quickly decreased rather than the positive components. As shown in Fig. 4(c), the distributed flexural wave velocity has two principal crests and one principal trough. As time further increases, the dispersive feature of the flexural wave in the circular plate causes more crests and troughs, as illustrated in Figs. 4(d) and (e). Due to the flexural wave speed of the component with the highest frequency in the wave packet, the flexural wave velocity distributes the whole observation range ($0\,\mathrm{m} \leqslant r \leqslant 5\,\mathrm{m}$) of the circular plate at $t = 0.034\,\mathrm{s}$ (Fig. 4(e)). It is worth noting that it seems that the wave components in velocity distribution spread out with faster speeds than those in displacement

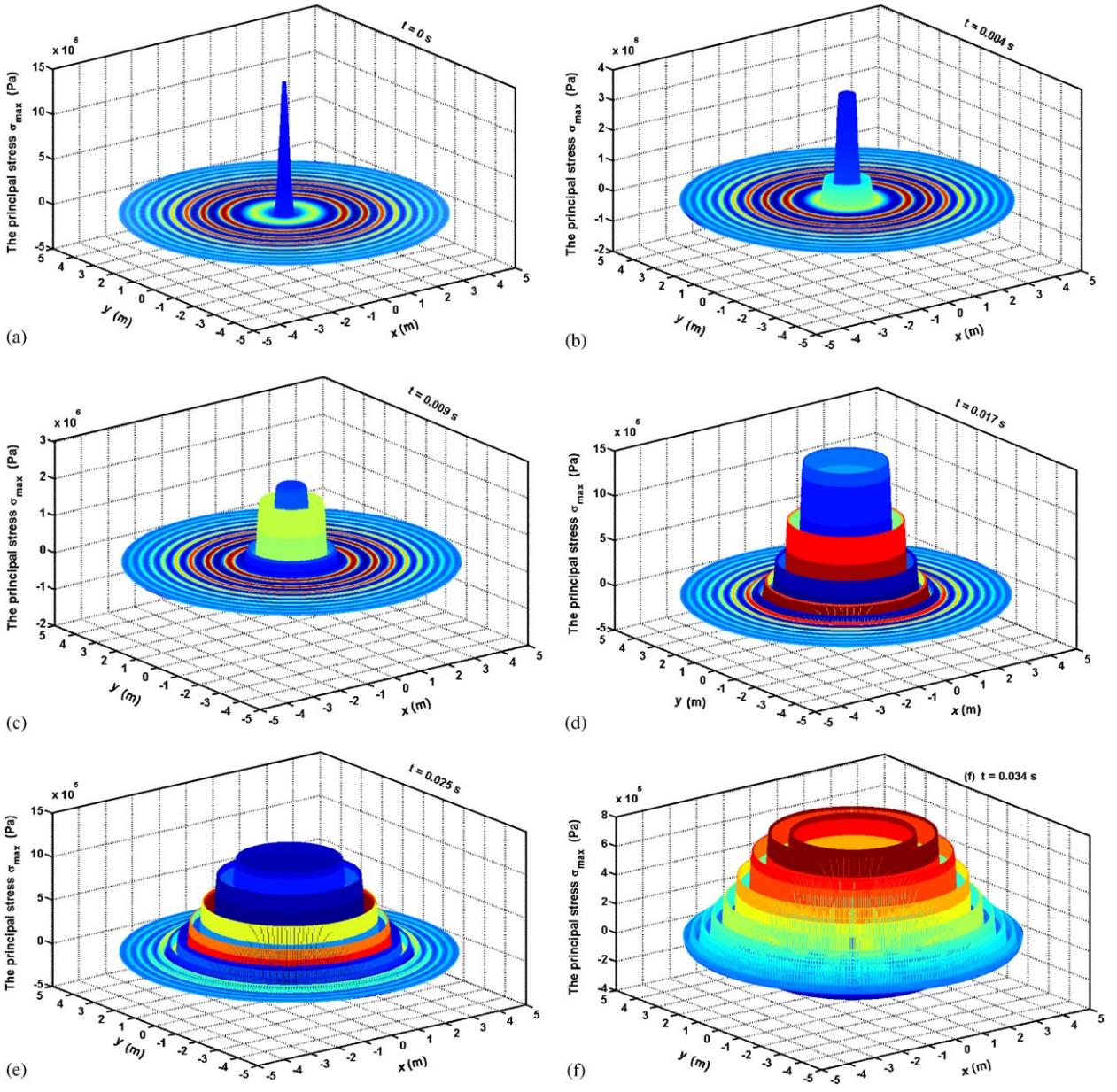

Fig. 6. Distribution of the principal stress at different instants by the AWP technique.

distribution. At the same instant, the wave speed of the component of the velocity (shear force, bending moment, stress and so on) is the same as that of the displacement. The difference in magnitude causes this wrong impression.

It would be useful to compare the different between ansiymmetrical wave propagation with wave propagation in one-dimensional flexural beam with the same thickness and material properties to the circular plate. For this comparison, the wave propagation of an infinite beam with the same initial disturbance is now considered. The general result of the displacement has the following form [16]:

$$w(x,t) = \frac{f_0}{(1+\tau^2)^{1/4}} e^{(-x^2/4\sigma^2(1+\tau^2))} \times \cos\left\{\left[\frac{x^2\tau}{4\sigma^2(1+\tau^2)}\right] - \frac{1}{2}\tan^{-1}(\tau)\right\}, \tag{43}$$

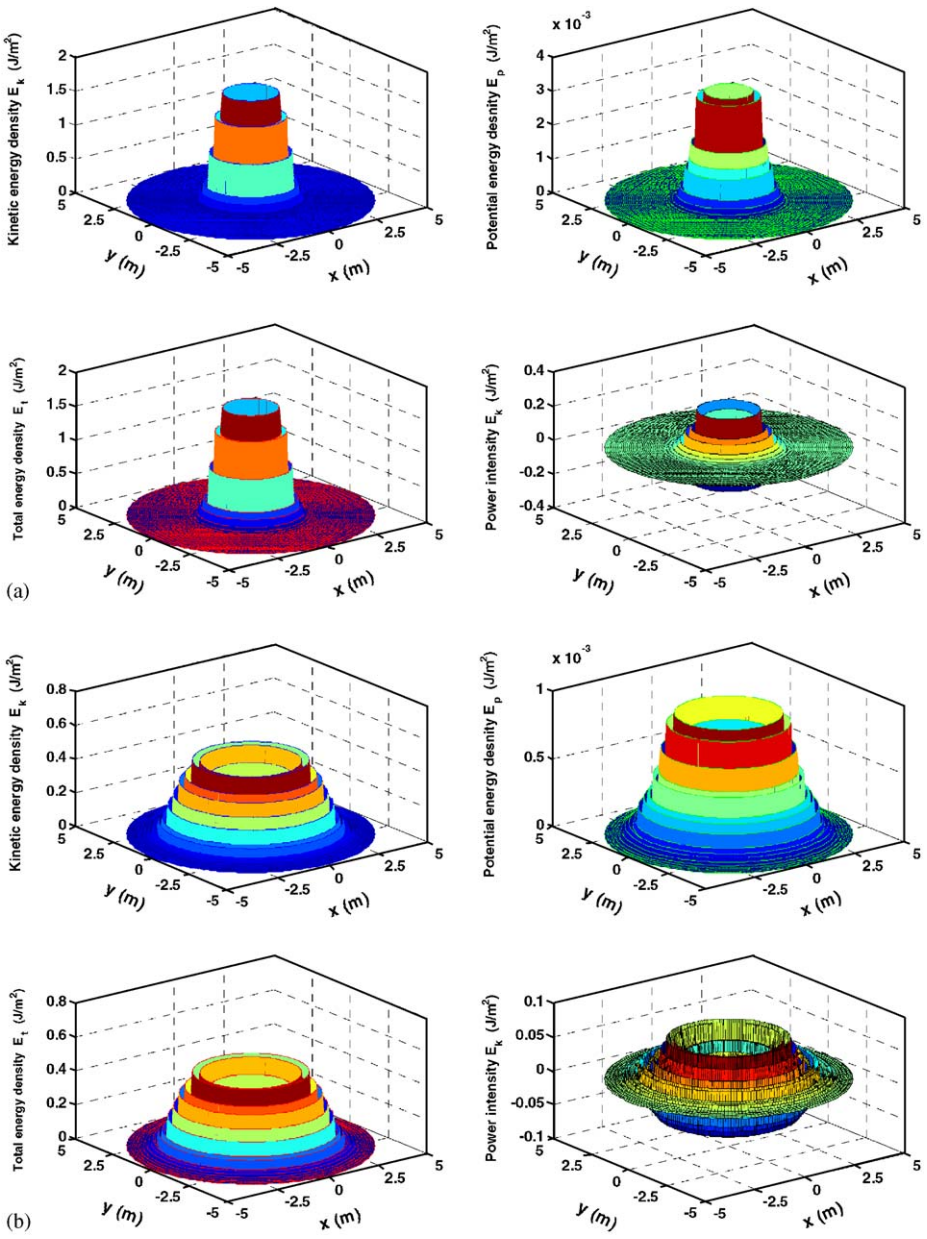

Fig. 7. Distribution of energy densities and power intensity at two different instants.

where $\tau = b't/\sigma^2$, the coefficient b' can be calculated by $\sqrt{EI/\rho A} = \sqrt{Eh^2/12\rho}$; $w(x,t)$ represents the deflection displacement of the flexural beam in the z-axis; and σ and f_0 have the same values as those given in Eq. (38).

The accuracy comparison for the Chebyshev–Fourier scheme with the above exact analytical solution (Eq. (43)) has been described in Ref. [17]. Here, the displacement difference between the circular plate and one-dimensional flexural beam at three different instants is shown in Fig. 5 based on the same simulated

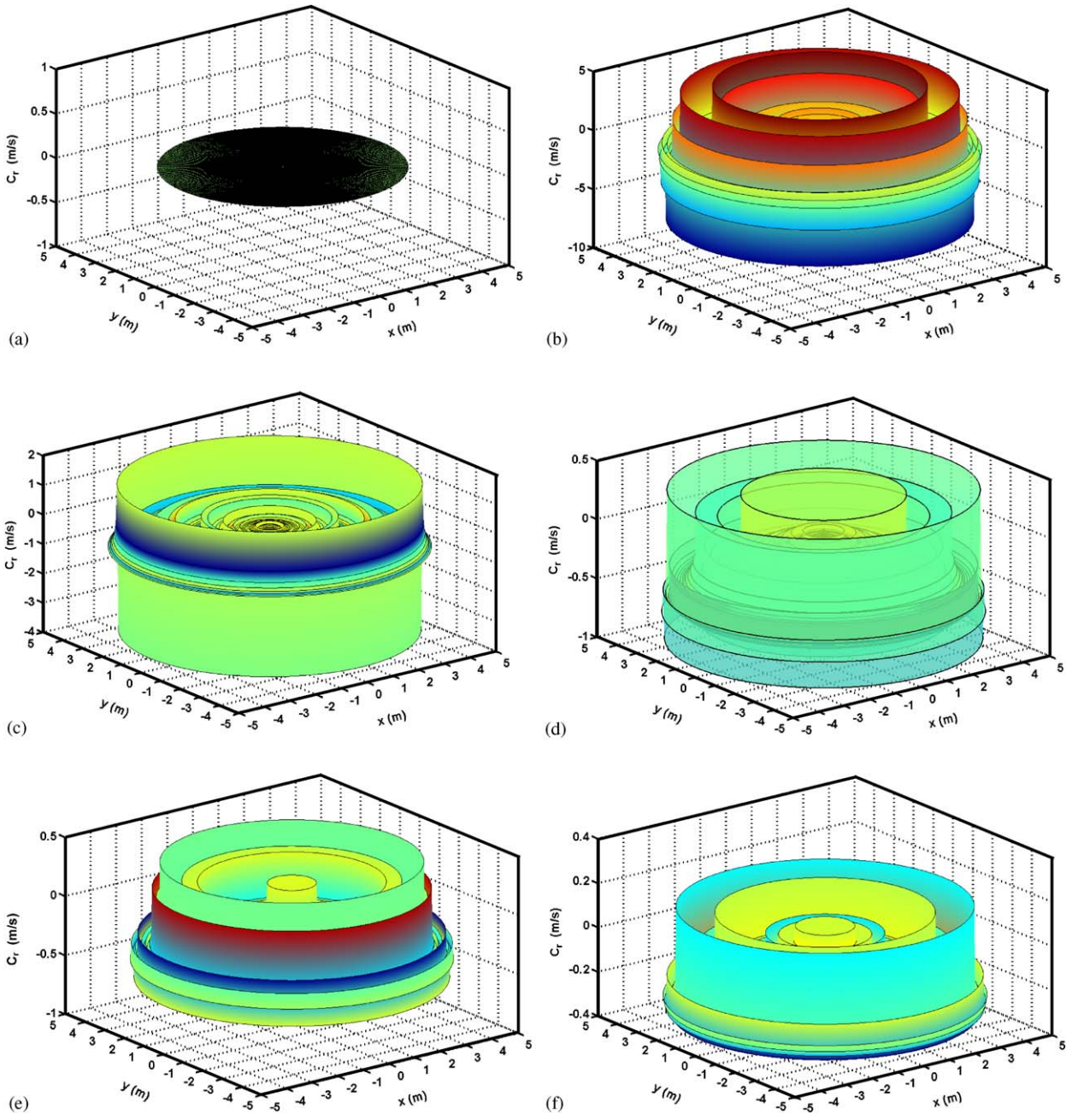

Fig. 8. Coefficients of energy densities and power intensity at different instants.

parameters and initial impulse (Fig. 5(a)). At $t = 0.017$ s, although the material properties and simulated parameters including the initial wave packet are kept the same, the wave propagation patterns are much different, which can reflected by the comparison of the maximum magnitudes of beam displacement (0.4 mm in Fig. 5(b) and 0.3 mm in Fig. 5(c)) and those of the circular plate (0.15 mm in Fig. 5(b) and 0.04 mm in Fig. 5(c). It is worth noting that the propagation velocities along the radius direction (not vibrating flexural velocity along z direction) are a slight different between the beam and circular plate because Poisson's ratio υ is considered in the circular plate $D = Eh^3/12(1-\upsilon^2)$. If the effect of Poisson's ratio υ is neglected, then the distributed flexural wave displacements have only difference in magnitudes, not phases, between the circular plate and the beam.

Fig. 6 shows the principal stress distribution at six different instants. Compared with patterns in Figs. 3 and 4, the principal stress has the similar distribution as Fig. 3 at $t = 0$ and 0.004 s except the difference in magnitude. The initial stress is concentrated on the centre of this structure. As time increases, the principal stress spreads out with decreased magnitude as illustrated in Figs. 6(b)–(f). It is noted that the principal stress has similar distribution as velocity rather than displacement at later instants.

Fig. 7 shows distributions of energy densities and power intensity at two different instants. At $t = 0.017$ s, the kinetic energy density has the similar distribution as the velocity except in magnitude. It is noted that the kinetic energy density just consists of positive component (crests). Compared with the kinetic energy density, the potential density has much smaller magnitude, as shown in Fig. 7(a). Therefore, the total energy density has the same pattern as the kinetic density. The power intensity has the larger (100 times) magnitude than the potential density, and the small (10 times) magnitude than the kinetic density, as shown in Fig. 7(a). At $t = 0.034$ s, the magnitude of the kinetic energy density decreases quickly, especially the central crests. Similarly, the potential density has negligible magnitude compared with the kinetic density, as shown in Fig. 7(b). The total energy density is dependent on the kinetic density. The power intensity has the similar distribution as the total energy density except in magnitude at the instant $t = 0.034$ s. Generally, the above analysis will help to obtain a good understanding of effects of kinetic energy and potential energy densities on the total energy density.

Fig. 8 illustrates the distribution of coefficients of energy densities E_k, E_p, E_t, and power intensity I_r at six different instants. The unit of the coefficient C_r is m/s. At $t = 0$ s, the coefficient C_r is zero because the initial velocity is zero (Eq. (15)). As time increases, at $t = 0.006$ s, the power intensity I_r is larger than the total energy E_t as shown in Fig. 8(b). Each circular curve presents propagating frequency component. It is noted that Fig. 8(c) shows much different distribution. Near the edge of the plate, the coefficient C_r has much larger value than other frequency components. After $t = 0.009$ s, the coefficient is less than 1, and then gradually decreases. Above analysis will help to obtain a thorough understanding of the relationships among kinetic energy, potential energy densities, and the total energy density.

4. Conclusions

In this paper, the acoustical wave propagator (AWP) technique is extended to describe the time-domain evolution of wave packet in a circular plate in polar coordinates. A Chebyshev polynomial expansion scheme is implemented to carry out the operation of the AWP in polar coordinates. Compared with exact analytical solution of velocity, this scheme is found to be accurate and computationally effective for the prediction of the time-domain evolution of acoustical waves. The coefficient of the power intensity and energy density is described in details. The above analysis is helpful to get a good understanding of the relationship between the kinetic energy, potential energy, the total energy and power flow.

Acknowledgements

The authors are grateful to Dr. K.S. Sum for his valuable discussion and Asst. Professor J.B. Wang for her help in numerical analysis. The first author thanks the financial supports from the University Whitfeld Fellowship provided by the University of Western Australia, and the Hong Kong Polytechnic Postdoctoral Fellowship by the Hong Kong Polytechnic University.

References

[1] G.C. Pardoen, R.L. Hagen, Symmetrical bending of circular plates using finite elements, *Computers and Structures* 2 (1972) 547–553.
[2] G.C. Pardoen, Static vibration and buckling analysis of axisymmetric circular plates using finite elements, *Computers and Structures* 3 (1973) 355–375.
[3] H. Schmidt, S. Krenk, Asymmetric vibration of a circular elastic plate on an elastic half space, *International Journal of Solids and Structures* 18 (1982) 91–105.
[4] T.P. Chang, Statistical analysis of a circular plate on a random winkler foundation, *Computers and Structures* 48 (1993) 161–166.
[5] J.S. Chang, Axisymmetric buckling of moderately thick polar orthotropic plates, *Composites Science and Technology* 52 (1994) 73–83.
[6] V. Mermertas, H.T. Belek, Stability of variably thick orthotropic annular plates, *International Journal of Mechanical Sciences* 36 (1994) 737–749.
[7] P.K. Roy, N. Ganesan, Dynamic stress analysis of a tapered clamped-free annular circular plate under axisymmetric impact load, *Journal of Sound and Vibration* 178 (1994) 681–687.
[8] C.M. Wang, Relationships between Mindlin and Kirchhoff bending solutions for tapered circular and annular plates, *Engineering Structures* 19 (1997) 255–258.
[9] K.M. Liew, J.B. Han, Z.M. Xiao, Vibration analysis of circular Mindlin plates using the differential quadrature method, *Journal of Sound and Vibration* 205 (1997) 617–630.
[10] C.L. Chang, Z.Y. Lee, Applying the double side method of weighted residual for solving circle plate large deformation problems, *Applied Mathematics and Computation* 141 (2003) 477–490.
[11] J. Pan, J.B. Wang, Acoustical wave propagator, *The Journal of the Acoustical Society of America* 108 (2002) 481–487.
[12] S.Z. Peng, J. Pan, Acoustical wave propagator for time-domain flexural waves in thin plates, *The Journal of the Acoustical Society of America* 115 (2004) 467–474.
[13] S.Z. Peng, J. Pan, A study of time-domain dynamic stress concentration in a plate with a sharp change of section using acoustical wave propagator technique, *The Journal of the Acoustical Society of America* 117 (2005) 492–502.
[14] S.Z. Peng, Dynamic stress concentration in a ribbed plate using acoustical wave propagator technique, *Journal of Sound and Vibration* 279 (2005) 75–88.
[15] S.Z. Peng, Flexural wave scattering and dynamic stress concentration in a heterogeneous plate with multiple cylindrical patches by the improved acoustical wave propagator technique, *Journal of Sound and Vibration* 286 (2005) 729–743.
[16] K.F. Graff, *Wave Motion in Elastic Solids*, Clarendon Press, Oxford, 1975.
[17] S.Z. Peng, J. Pan, Acoustical wave propagator technique for time-domain reflection and transmission of flexural wave packets in one-dimensional stepped beams, *Journal of Sound and Vibration*, accepted for final publication.